AIAA JOURNAL
Vol. 39, No. 8, August 2001

Development of Piezoelectric Actuators for Active Flow Control

Louis N. Cattafesta III,* Sanjay Garg,† and Deepak Shukla†
High Technology Corporation, Hampton, Virginia 23666

The development of piezoelectric actuators for active flow control is discussed. The type of actuators considered consists of a single sheet of piezoceramic material bonded to the underside of a shim: a "unimorph" flap design. Existing theoretical beam models are extended to incorporate a linear strain distribution in the composite unimorph beam structure. This model is combined with an optimization scheme to design a flap that maximizes the tip deflection per unit voltage for a given bandwidth. The optimization model is then used to design a piezoelectric actuator. The model predictions compare favorably to measurements of the actuator frequency response function. A sample application to control of separated flow from a backward-facing step is also described, in which the actuator is installed at the origin of the free shear layer. Detailed hot-wire measurements, together with dimensional analysis, reveal the physical mechanism responsible for the fluid-structure coupling. A quasi-static model based on the solid-body displacement of the incoming shear layer accurately describes the peak streamwise velocity perturbations produced by the actuator. This model leads to a proportional relationship between the flap tip displacement, the incoming boundary-layer profile parameters, and the streamwise velocity fluctuations produced by the actuator.

Introduction

ADVANCES in the understanding of the important role of coherent structures in fluid dynamics have provoked interest in the field of active flow control. Work in this area has been further aided by recent developments in control theory and microfabrication technology.[1] The potential applications are diverse and technologically significant: drag reduction, noise abatement, separation control, mixing enhancement, etc.

In a general application a modern active flow control system consists of sensors, actuators, and a control system. The controller receives information regarding the state of the flow from the sensors and processes it to determine the appropriate control signal for the actuators. Such a controller could be based on 1) a physically realistic reduced-order flow model, 2) system identification techniques, or 3) a nonparametric, self-learning scheme (e.g., neural networks).

The desired characteristics of actuators to be used in the fashion just outlined include low power consumption, fast time response, reliability, and low cost. They must also be capable of introducing a significant disturbance into the flow when activated. Thus, an understanding of the fluid-structure coupling is of paramount importance. Piezoelectric materials, which develop mechanical strain in response to an applied electric field (and vice versa), are potentially suitable as actuators for flow-control applications. Indeed, actuators fabricated from such materials are now widely used in the area of structural vibration control and are making inroads in the flow-control community. Piezoelectric actuators were first used for flow control by Wehrmann in the mid-1960s.[2–4] However, their utility in practical situations was limited as a result of the reduction in their response far from their natural frequency. Wiltse and Glezer devised a clever excitation scheme that employed amplitude modulation (AM) of a resonant carrier waveform.[5] Their technique allowed for effective excitation of free-shear flows away from the natural frequency of the actuators. Jacobson and Reynolds have also recently applied this technique to wall-bounded flows.[6]

Because the amplitude-modulated approach requires that the actuator be driven at its natural frequency, the probability of mechanical failure is greater than for an off-resonance design. Furthermore, AM resonant actuators may not be appropriate for use in some shear flows as a result of the necessity of using complex periodic signals. In particular, it is well known that free shear flows are unstable to excitation at frequencies ranging from dc to some upper limit f_{max}, which scales directly with flow speed and inversely with a characteristic length scale of the flow (e.g., shear-layer momentum thickness). Therefore the flow can be unstable at the natural frequency of the actuator, and AM excitation can result in the introduction of undesirable disturbances in the flow.

This paper discusses the development of piezoelectric flap actuators that produce significant flow disturbances at frequencies ranging from dc to their first natural frequency. As will be shown, if properly designed, such a piezoelectric actuator behaves like a second-order system at frequencies near and below its fundamental mode. This implies that the frequency response (both amplitude and phase) will be approximately flat at frequencies well below the natural frequency. A flat phase response is desirable in the control of flow phenomena that are sensitive to the phase of the control input, particularly when arrays of actuators are used. These requirements emphasize the importance of a design methodology that properly accounts for the dynamic response of the actuators. This has only recently been addressed for zero-net mass flux actuators that are used near their fundamental resonance frequency.[7]

This paper focuses on the development of design tools for piezoelectric unimorph flap actuators suitable for active flow control. To design effective piezoelectric actuators, two problems must be considered. First, a suitable structural dynamics model of the actuator is identified, and the actuator design is recast as an optimization problem to maximize the actuator tip displacement per unit volt while matching a prescribed natural frequency. Second, and perhaps more significantly, a model that accounts for the coupling between the actuator and the large-scale fluid motion is addressed. In this case we seek to identify a scaling law that relates the actuator tip displacement to streamwise velocity perturbations induced in the flow.

The paper is arranged as follows. A simple beam model for estimating the dynamic response of a unimorph cantilever actuator is described. The formulation of the design-optimization problem follows. The model predictions are then compared to measurements of the frequency response of prototype devices that were designed using the optimization method. Next a flow-control application is described in which these actuators were installed in a backward-facing step at the origin of a free shear layer. The results of hot-wire measurements of the open-loop controlled flow in the immediate vicinity of the actuator tip are described. These results lead to a proposed scaling law that relates actuator tip displacement to induced velocity fluctuations.

Received 25 March 2000; revision received 1 February 2001; accepted for publication 26 February 2001.

*Senior Research Scientist; currently Assistant Professor, Department of Aerospace Engineering, Mechanics, and Engineering Science, University of Florida, 141 NEB, P.O. Box 116250, Gainesville, FL 32611-6250; catman@aero.ufl.edu. Senior Member AIAA.

†Research Scientist, 28 Research Drive.

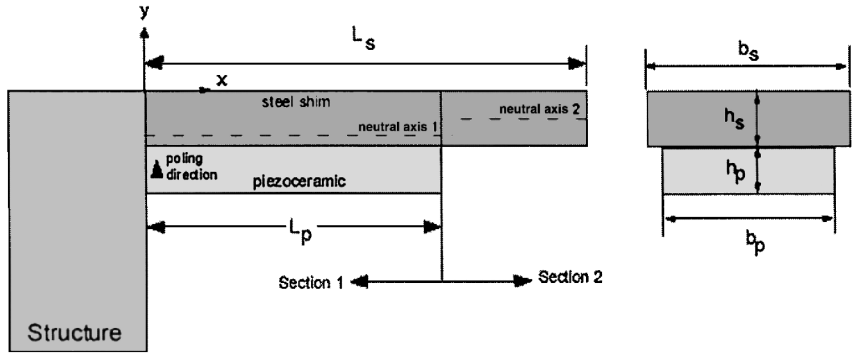

Fig. 1 Schematic of Euler–Bernoulli beam model for piezoelectric unimorph actuator.

Actuator Model

Piezoelectric actuators designed for fluid-flow applications can take many forms. The particular configuration studied consists of a piezoceramic material bonded to the underside of a metal shim, as shown in Fig. 1. Most installations require that the actuator does not protrude significantly into the flow in order to avoid a substantial drag penalty and to minimize the aerodynamic load on the actuator. Thus, the device is often flush mounted in the surface of a structure. In addition, it is often convenient for the shim material to be grounded electrically (for safety) because its surface is exposed. Such a device is termed a "unimorph" actuator, as opposed to the more conventional "bimorph" design used in structural control in which a shim is bonded to (and electrically isolated from) two piezoceramic sheets.

If the length of the actuator is large compared to both its width and thickness, then the structure can be modeled as a beam.[8–10] Figure 1 shows a schematic of a cantilever beam, in which one end is clamped and the other is free. For the case in which the poling direction of the piezoceramic is in the $\pm y$ direction, the beam bends in the xy plane when a voltage is applied across the piezoceramic. Thus, the actuator introduces velocity fluctuations into a flow over its upper surface when driven by an appropriate ac voltage. From a design standpoint it is important to know a priori the performance characteristics of the actuator (e.g., its dynamic response) before significant time and effort is expended fabricating and testing the device.

The actuator is modeled using Euler–Bernoulli beam theory.[11] As shown in Fig. 1, the beam consists of two parts: a composite section consisting of a piezoceramic material perfectly bonded to a metal shim and a second section consisting of the shim only. Crawley and de Luis[12] and Won[13] showed that the effect of a perfectly bonded piezoceramic is to introduce a concentrated couple or moment at the end of the piezoceramic $x = L_p$. In structural applications the piezoceramic thickness is often small compared to that of the mating piece, permitting the assumption of a uniform strain distribution in the piezoceramic. But in flow-control applications the thickness of the piezoceramic is often comparable to the shim thickness. Therefore, for the general case of arbitrary piezoceramic and shim thickness, a linear strain distribution in the y direction is more appropriate and is adopted here, as shown in Fig. 2. The assumption of perfect bonding implies that the strain is continuous at the bond interface.[12] By definition, the strain is zero on the neutral axis for pure bending. Unlike the bimorph case the neutral axis is not symmetrically located within the beam. In addition, the model formulation imposes a discontinuity in the y location of the neutral axis at $x = L_p$ (Fig. 1).

Considering an element in the composite section, the governing differential equation for the beam deflection is obtained from a force balance in the y direction and a moment balance about the element:

$$(\rho_s b_s h_s + \rho_p b_p h_p)\frac{\partial^2 y_1}{\partial t^2} + \frac{\partial^2}{\partial x^2}\left[\left(E_s I_{s_1} + E_p I_p\right)\frac{\partial^2 y_1}{\partial x^2}\right] = \frac{\partial^2 M_0}{\partial x^2} + p_1(x,t) \tag{1}$$

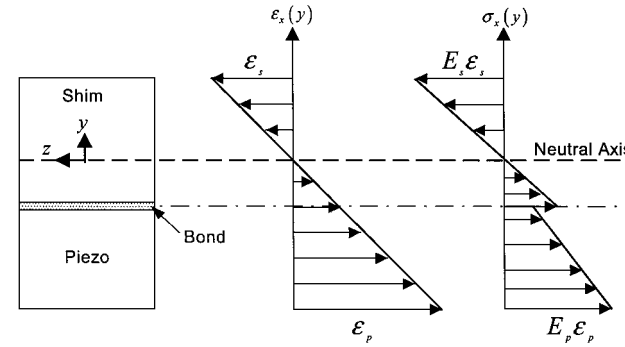

Fig. 2 Assumed linear strain distribution and corresponding normal stress in the (y, z) plane of the actuator.

where ρ is the density, E is the elastic modulus, I is the moment of inertia about the local neutral axis of the beam section, M_0 is the moment induced by the application of an electric field, and t is time. The subscripts p and s denote the piezoceramic and shim portions of the beam, respectively. The subscripts 1 and 2 correspond to the composite and shim sections, respectively.

The term $p_1(x, t)$ is the vertical load per unit length on the beam. If the reasonable assumption is made that horizontal shear forces caused by an adjacent fluid flow are negligible, then this term represents the aerodynamic pressure loading on the actuator. A thorough analysis requires a coupled fluid-structural model, in which $p_1(x, t)$ is the differential pressure acting on the actuator. Furthermore, the motion of the actuator alters the boundary conditions of the flow in a time-dependent manner. Unfortunately, such an approach is beyond the scope of the present work. Instead, we note that the fluid loading scales with the dynamic pressure $\rho U_\infty^2/2$ of the flow over the surface of the actuator. For air, we can express this term as $\gamma p_\infty M_\infty^2/2$, which is negligible at low Mach numbers. As a result, $p_1(x, t)$ is neglected.

Assuming a solution of the form $y_1(x, t) = y_1(x)e^{j\omega t}$ when driven by a harmonic electric field of angular frequency ω, constant properties along the length of the composite beam section, the governing equation simplifies to

$$\frac{\partial^4 y_1}{\partial x^4} - \beta_1^4 y_1 = 0 \tag{2}$$

where the wave number β_1 is defined as

$$\beta_1^4 = \frac{\omega^2(\rho_s b_s h_s + \rho_p b_p h_p)}{E_s I_{s_1} + E_p I_p} \tag{3}$$

The term $\partial^2 M_0/\partial x^2$ is zero everywhere except at $x = L_p$; its influence is imposed by the "matching" conditions there. The general solution to this differential equation takes the form

$$y_1(x \le L_p) = a_1 e^{j\beta_1 x} + a_2 e^{-j\beta_1 x} + a_3 e^{\beta_1 x} + a_4 e^{-\beta_1 x} \tag{4}$$

A similar analysis for section 2 in Fig. 1 yields a governing equation of the form

$$\frac{\partial^4 y_2}{\partial x^4} - \beta_2^4 y_2 = 0 \tag{5}$$

where the wave number β_2 is defined as

$$\beta_2^4 = \frac{\omega^2(\rho_s b_s h_s)}{E_s I_{s_2}} \tag{6}$$

Again, the solution takes the form

$$y_2(L_p \le x \le L_s) = a_5 e^{j\beta_2 x} + a_6 e^{-j\beta_2 x} + a_7 e^{\beta_2 x} + a_8 e^{-\beta_2 x} \tag{7}$$

The eight unknown coefficients $a_1, a_2, \ldots a8$ are determined by the four boundary conditions

$$y_1(x=0) = 0, \qquad y_1'(x=0) = 0$$
$$y_2''(x=L_s) = 0, \qquad y_2'''(x=L_s) = 0 \tag{8}$$

and the four matching conditions at the junction of the two sections $x = L_p$:

$$y_1(x=L_p) - y_2(x=L_p) = 0$$
$$y_1'(x=L_p) - y_2'(x=L_p) = 0$$
$$\left(E_s I_{s_1} + E_p I_p\right) y_1''(x=L_p) - E_s I_{s_2} y_2''(x=L_p) = M_0$$
$$\left(E_s I_{s_1} + E_p I_p\right) y_1'''(x=L_p) - \dot{E}_s I_{s_2} y_2'''(x=L_p) = 0 \tag{9}$$

where

$$M_0 = \int y\sigma(y)\,\mathrm{d}A = -\frac{1}{2} E_p d_{31} E_{\text{field}} b_p h_p (2h_{n1} - h_p) \tag{10}$$

is the effective applied moment caused by the piezoceramic patch and

$$h_{n1} = \frac{E_s b_s h_s^2 + 2E_s b_s h_s h_p + E_p b_p h_p^2}{2(E_s b_s h_s + E_p b_p h_p)} \tag{11}$$

is the distance from the bottom of the piezoceramic patch to the location of the neutral axis in section 1, d_{31} is the piezoelectric strain coefficient, and E_{field} is the magnitude of the applied electric field. Here, $d_{31} E_{\text{field}}$ is what is commonly called the induced strain caused by the piezoceramic.

As shown in Fig. 2, the location of the neutral axis in section 1 is determined by noting that $\int \sigma(y)\,\mathrm{d}A = 0$ for a cross section of the actuator and yields Eq. (11). The expression for M_0 is obtained by integrating the moment of the normal stress distribution over the same cross section. It is important to note that M_0 is different (by more than a factor of 2) from the symmetric bimorph value given in Crawley and de Luis.[12] They assume a uniform strain exists in the piezoceramic, which results in a different neutral axis location than for the bending case considered here. A uniform strain assumption is appropriate for piezoceramic patches of negligible thickness compared to the shim. However, in many flow control applications the thickness of the piezoceramic is not negligible, and a linear strain distribution is therefore used to simulate bending. The ratio of the applied moment for the linear strain distribution (shown in Fig. 2) to that for the uniform strain case considered in Crawley and de Luis is given by

$$\frac{M_{0_{\text{bending}}}}{M_{0_{\text{uniform}}}} = \frac{1/E_p/E_s(t_p/t_s)^2}{1 + [1 + (t_p/t_s)]} \tag{12}$$

For example, this ratio is about 0.82 for the actuator dimensions listed in Table 1.

The boundary conditions in Eq. (8) are standard for a cantilever beam with no load or moment applied at the tip of the beam. The first two matching conditions in Eq. (9) reflect the fact the beam deflection and slope are continuous at $x = L_p$. At this location the effective flexural rigidity EI of the beam sections is discontinuous.

Table 1 Details of piezoelectric unimorph actuator

Quantity	Value
Shim length L_s, mm	38.1
Piezo length L_p, mm	25.2
Shim thickness h_s, mm	0.254
Piezo thickness h_p, mm	0.33
Shim width b_s, mm	50.8
Piezo width b_p, mm	44.45
Shim density ρ_s, kg/m^3	8000
Piezo density ρ_p, kg/m^3	7500
Shim elastic modulus E_s, N/m^2	2.0×10^{11}
Piezo elastic modulus E_p, N/m^2	6.2×10^{10}
Piezo strain constant d_{31}, m/V	-274×10^{-12}

Thus the flexural rigidity terms are required in the last two matching conditions of Eq. (9), which express the discontinuity in the bending moment and vertical shear in terms of the beam shape.

As shown in Appendix A, the eight conditions can be written in matrix form as

$$D \cdot A = b \tag{13}$$

The homogeneous solution for the case in which no electric field is applied is an eigenvalue problem in which the values of the wave numbers β_1 and β_2 that make $|D| = 0$ define the natural frequencies of the actuator. The matrix solution to the forced problem, in which a sinusoidal electric field is applied, provides an estimate of the undamped dynamic response of the actuator $y_1(x, \omega)$ and $y_2(x, \omega)$.

The benefit of the preceding approach is that it allows one to estimate the dynamic response of the unimorph actuator without having to assume a mode shape (the approach taken by Crawley and de Luis[12]). The model will be shown to be sufficiently accurate for design purposes. As a result, the preceding formulation, when combined with the design optimization scheme described next, makes the flow-control actuator design problem tractable.

Design Optimization Scheme

In a flow-control application a user may wish to design an actuator with a specific fundamental resonant frequency while simultaneously seeking to maximize its tip deflection per unit voltage. Additional size constraints (e.g., weight) can also be imposed. To address this problem, a design optimization algorithm was developed. In particular, given shim and piezo material properties and their widths, an algorithm was implemented that iteratively adjusts the thickness of the shim and the location, thickness, and length of the piezo to achieve a desired natural frequency with maximum tip deflection per unit voltage. The cost function that is minimized is given by

$$J = W_F[(F_{\max} - F_{\max,\text{desired}})/F_{\max,\text{desired}}]^2 + W_{\text{def}}[H(0) \cdot 1V/L_s]^2 \tag{14}$$

where $F_{\max}$ is the resonant frequency, $F_{\max,\text{desired}}$ is the desired resonance frequency, $H(0)$ is the magnitude of the frequency response function at zero frequency between the applied voltage and the resulting tip deflection (its units are m/V), and L_s is the user-specified length of the shim (see Fig. 1). The quantity $[H(0)(1V)/L_s]$ is a nondimensional tip displacement caused by a unit applied voltage. W_F and W_{def} are nondimensional weights that are adjusted by the user to make the cost function approximately equally sensitive to the frequency and tip deflection terms.

By inspection, it is clear that minimizing J is accomplished by matching the desired frequency exactly and by maximizing the tip deflection. This algorithm enables one to quickly design a flap-type actuator to meet specific displacement and bandwidth requirements. The algorithm employed uses the simplex direct search method described by Lagarias et al.[14]

A piezoelectric unimorph actuator was designed using the preceding model and optimization algorithm. The specific objective of this design was to optimize the length of the piezoceramic L_p in order to achieve a desired resonant frequency of 300 Hz. Starting from a random initial guess, the optimization algorithm converged

in approximately 50 iterations. Table 1 provides a summary of the dimensions and property values of the actuator. The width of the actuator is greater than its length, a configuration that inevitably results in some anticlastic curvature that is characteristic of a rectangular plate with a small length-to-width ratio. Nonetheless, the centerline deflection is accurately modeled via Euler–Bernoulli beam theory.

Results and Discussion

Frequency Response Measurements

The design summarized in Table 1 was fabricated for bench-top and wind-tunnel testing. Epoxy adhesive was used to bond the stainless-steel shim to the piezoceramic. The following experimental setup was used for the bench-top frequency response tests. Broadband random noise from a function generator was passed through a low-pass elliptic filter ($f_c = 2$ kHz) and a power amplifier possessing a nominal gain of 150. The resulting band-limited random noise was used as the input signal to the actuators. The midplane actuator tip deflection was measured with a fiber-optic displacement sensor. The two channels were low-pass filtered at 2 kHz and sampled at 10 kHz with a 16-bit A/D converter. The resulting signals were analyzed to produce the frequency response function and coherence between the input voltage and output displacement. For the spectral analysis, 4 K fast Fourier transforms, a Hanning window with no overlap, and 100 averages were used to ensure negligible bias and random errors. The linear coherence function was near unity for the entire bandwidth. The 95% uncertainty estimate in the frequency responce function is 2.5% near the resonance frequency, and the frequency resolution is 2.44 Hz. For the measurements presented next, a positive voltage represents a deflection in the $-y$ direction (see Fig. 1 for coordinate system).

Figure 3 displays the predicted and measured frequency response of the actuator for frequencies up to the fundamental mode. The agreement between the model predictions and measurements is quite good. The measured and predicted resonance frequency were 320 and 306 Hz, respectively. The measured and predicted low-frequency value (i.e., dc response) of the frequency response magnitude were 0.0014 and 0.0013 mm/V, respectively. The overall agreement between the predicted and actual response is satisfactory. Because the desired operating condition of the actuator lies from dc to around the natural frequency, the design optimization scheme is therefore sufficient for design purposes. However, additional research is required to characterize the full-field dynamic displacement characteristics of the actuator.

A curve fit to a second order system is also shown in Fig. 3. The curve fit is expressed as

$$H(\omega) = K_0 \Big/ \left\{ \left[1 - (\omega/\omega_n)^2 \right] + j[2\xi(\omega/\omega_n)] \right\} \qquad (15)$$

where K_0 is the dc response or gain, ω_n is the angular natural frequency, and ξ is the damping ratio. The fitted values of K_0, ω_n, and ξ are 0.0014 mm/V, 1995 rad/s (319 Hz), and 0.017, respectively. (Note that the beam model does not include damping; however, the model work well because the damping in the system is small. Also, the predicted response is infinite at the natural frequency. This is not apparent in Fig. 3 because the resolution of the calculated frequency response is 10 Hz.) The low damping ratio value validates the model assumption of negligible damping, but its exclusion precludes the possibility of predicting the structural response at resonance.

Fluid-Structure Coupling Model

This section addresses the important question of how the actuator motion couples with the large-scale motion of the flow. In particular, given some knowledge of an actuator's displacement characteristics,

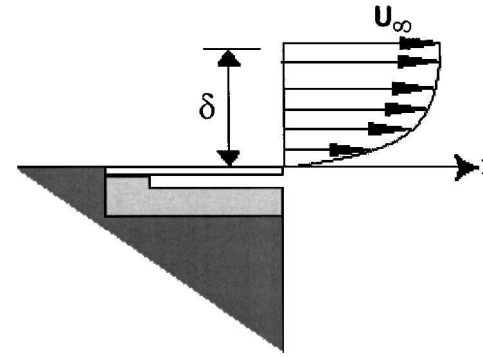

Fig. 4 Installation of flap actuator in backward-facing step.

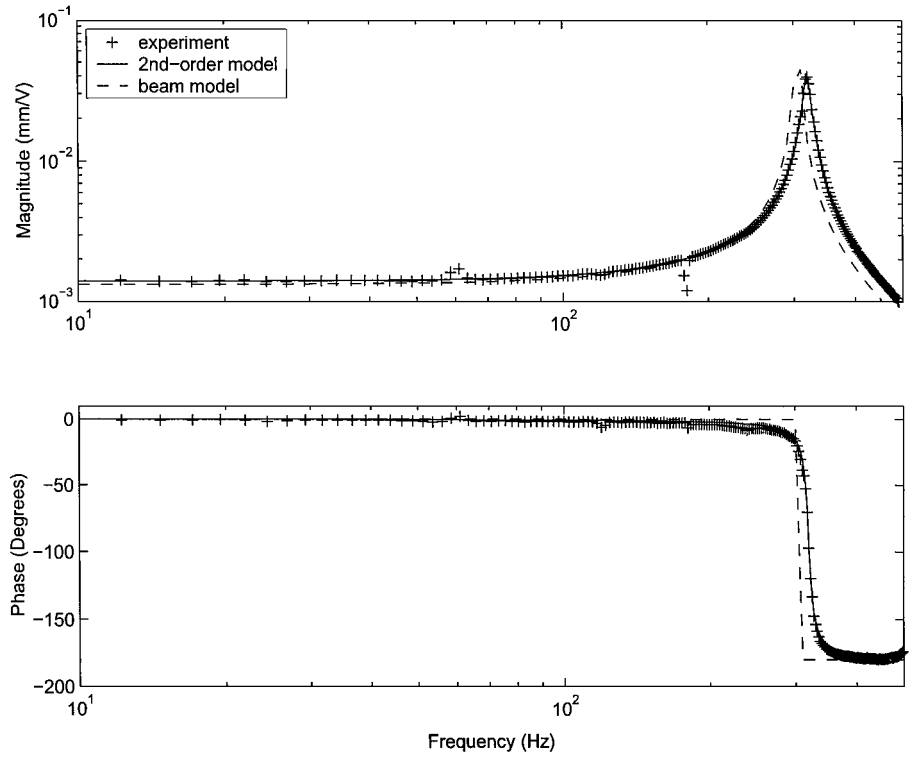

Fig. 3 Comparison between beam model, measured frequency response, and fitted second-order model.

it is important to be able to estimate the magnitude of the velocity perturbation that the actuator can produce. In an effort to answer this question, the actuator just described was installed in a backward-facing step as shown in Fig. 4. The backward-facing step models many practical flow control problems, such as separation control. The tip of the flap coincides with the separation location of a flat-plate turbulent boundary layer. The turbulent boundary layer has a thickness of $\delta = 24.7$ mm, a momentum thickness of $\theta = 2.1$ mm, and a Reynolds number based on momentum thickness of $Re_\theta = 5.2 \times 10^3$. A $23.8V_{\text{rms}}$ sinusoid at 256 Hz was used to power the actuator and excite the flow. Because of negligible aerodynamic loading in this low-speed flow, the in situ measured frequency response function was essentially identical to that measured in the absence of flow.

The mean and fluctuating components of the streamwise velocity were measured with a constant-temperature hot-wire anemometer. The hot wires were calibrated in situ over the entire speed range of the wind tunnel ($\sim 1 - 53$ m/s) for various ambient freestream temperatures. The data were reduced using the technique of Cimbala and Park,[15] which uses a nonlinear parametric curve fit that accounts for freestream temperature variations. The mean component of the hot-wire signal was measured using a high-precision integrating

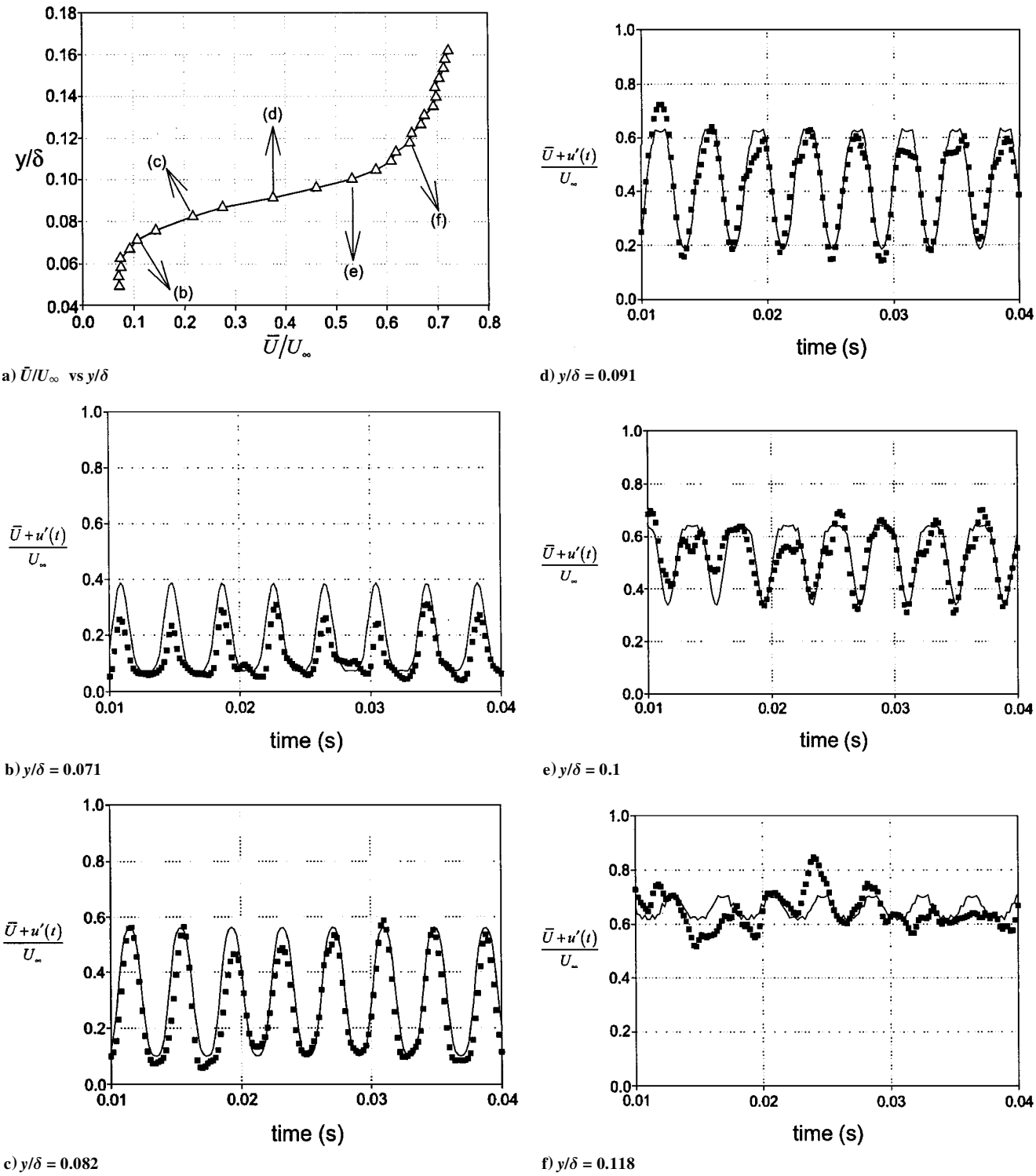

Fig. 5 Fluid-structure coupling model for flap actuator: a) mean streamwise velocity profile $\bar{U}/U_\infty$ vs normalized vertical distance y/δ from the separation location; b)–f) time-resolved traces $U(t,y)/U_\infty = [\bar{U}(y) + u'(t,y)]/U_\infty$ at the locations indicated in panel a): ■, data, and ——, Eq. (17) model.

voltmeter, whereas the ac component was obtained by bandpass filtering the signal from 1 Hz to 2 kHz and sampling at 5 kHz with a 16-bit A/D converter. The estimated uncertainty in the hot-wire velocity mesurements, avaraged over the entire velocity range, is 2.2%.

An examination of the data revealed that the calculated tip velocity (= tip displacement amplitude $\times\,\omega$) was one order of magnitude less than the amplitude of the peak velocity fluctuations measured just downstream of separation. For example, at the excitation frequency of 256 Hz, the measured tip displacement amplitude was approximately 0.4 mm, translating into a vertical velocity fluctuation of 0.64 m/s. The measured streamwise velocity fluctuations exceeded 10 m/s. This disparity indicates that the fluid-structure coupling is more involved than just estimating the tip velocity.

We hypothesize that the effect of the flap is to displace the boundary/shear layer in the y direction. This argument is based on an order-of-magnitude analysis of the ratio of the characteristic timescale of the large-scale structures in the turbulent boundary layer to that of the actuator forcing function:

$$\frac{\tau_{\mathrm{BL}}}{T} \approx \frac{\delta/U_\infty}{1/f} = \frac{f\cdot\delta}{U_\infty} \tag{16}$$

where $f = 256$ Hz is the frequency of the forcing, $\delta = 24.7$ mm is the boundary-layer thickness, and $U_\infty = 39.6$ m/s is the freestream speed. The value of the parameter $f\delta/U_\infty$ from Eq. (16) is 0.16, indicating that the quasi-static displacement assumption is valid for this case. As a result, the boundary layer is able to adjust quickly to the relatively slow periodic motion of the actuator. The net effect is to periodically displace the boundary layer in the y direction. Equation (16) is based on global scaling in the boundary layer and ignores potential interactions between the actuator and near-wall coherent structures.

Using this scaling argument, knowledge of the mean shear-layer velocity profile, the measurement location y, the angular frequency of the excitation ω, and the flap-tip displacement amplitude A_{tip} ($\sim$ 0.4 mm in the current example), the velocity perturbation seen by the wire is estimated as

$$u'(y,t) \cong \bar{U}[y + A_{\mathrm{tip}}\sin(\omega t)] - \bar{U}(y) \tag{17}$$

where $\bar{U}$ is the time-averaged, steamwise velocity profile that is only a function of y (the vertical distance from the actuator surface). Equation (17) effectively states that the actuator displaces the boundary layer in the y direction as if the boundary layer were a solid body. Therefore, the stationary hot-wire probe "sees" different velocity fluctuations depending upon its vertical location y in the layer.

Figure 5 corresponds to measurements approximately 1.6 mm downstream of the flap tip. The data in these figures were obtained by traversing the hot-wire probe in the y direction through the shear layer. The center of Fig. 5 shows a detailed plot of the mean velocity profile measured over a distance of less than 3 mm. As the hot-wire probe was traversed, time-resolved and time-averaged velocity data were obtained. In the surrounding plots excerpts are shown of the time-resolved normalized velocity $U(t,y)/U_\infty = [\bar{U}(y) + u'(t,y)]/U_\infty$, both measured and estimated from Eq. (17), at different y locations in the shear layer.

The agreement is quite good in the region of large shear and poor otherwise, indicating that the displacement effect just hypothesized is correct in the vicinity of large mean shear. This is perhaps surprising given that the boundary layer is turbulent. A comparison at lower levels of excitation provides similar results. Thus, the magnitude of the flap-induced perturbation into a shear layer is a function of both the flap-tip displacement and the mean velocity profile. Depending upon the location of the hot-wire probe, the resulting velocity perturbation can vary from a sinusoid, as in Fig. 5c, to a nonlinear, highly skewed disturbance, as in Figs. 5b and 5d.

It is now clear that in order to estimate the potential effectiveness of an actuator design some knowledge is required of the velocity profile of the uncontrolled flow. Analysis of the data in Fig. 5 indicates that an oscillating flap generates a maximum disturbance amplitude u'_{max} in the shear layer on the order of $A_{\mathrm{tip}}(\partial u/\partial y)_{\mathrm{max}}$, where $(\partial u/\partial y)_{\mathrm{max}}$ is the maximum value of the velocity gradient in the shear layer. For the case shown in Fig. 5, the disturbance amplitude $u'_{\mathrm{max}}/U_\infty$ is thus estimated as 0.26. This value compares favorably with the maximum measured disturbance amplitudes of approximately 0.25, as seen in Fig. 5.

The peak value $u'_{\mathrm{max}}/U_\infty$ in the shear layer can, in turn, be related to the incoming boundary-layer profile. In particular, it is proportional to $A_{\mathrm{tip}}\tau_{\mathrm{wall}}/\mu U_\infty = A_{\mathrm{tip}}C_f U_\infty/2\nu$, where τ_{wall} is the value of the wall shear stress just upstream of separation, μ is the dynamic viscosity, $\nu = \mu/\rho$ is the kinematic viscosity, and C_f is the nondimensional skin-friction coefficient. In this example, C_f can be related to the Reynolds number of the flow based on the incoming turbulent boundary-layer thickness δ via $C_f \approx 0.018 Re_\delta^{-1/6}$ (Ref. 16). As a result, the following proportional relationship between $u'_{\mathrm{max}}/U_\infty$, A_{tip}, and the boundary-layer parameters is obtained for the case of a flat-plate turbulent boundary layer:

$$\frac{u'_{\mathrm{max}}}{U_\infty} \propto \frac{A_{\mathrm{tip}} Re_\delta^{\frac{5}{6}}}{\delta} \quad \text{or} \quad \frac{u'_{\mathrm{max}}}{U_\infty} = \text{const}\,\frac{A_{\mathrm{tip}} U_\infty^{\frac{5}{6}}\delta^{\frac{-1}{6}}}{\nu^{\frac{5}{6}}} \tag{18}$$

where the proportionality constant is, using our limited data, approximately 0.00165.

The preceding scaling analysis assumes that the peak velocity gradient in the shear layer is proportional to the wall shear stress in the incoming boundary layer. Although only true in a qualitative sense, the benefit of this approach is that $u'_{\mathrm{max}}/U_\infty$ can be related to easily estimated quantities in the boundary layer (i.e., Re_δ). An alternate method, which might produce better quantitative estimates for $u'_{\mathrm{max}}/U_\infty$, would be to model the actuator disturbance velocity based upon the velocity profile in the logarithmic region of the boundary layer.

Nonetheless, the scaling analysis indicates that $u'_{\mathrm{max}}/U_\infty$ is strongly dependent on the actuator tip displacement and freestream velocity (as expected) but is only weakly dependent upon the boundary-layer thickness. Based on the limited current results and the preceding scaling analysis, it appears that significant velocity fluctuations can be produced by an oscillating flap, even in a relatively thick boundary layer, provided that aerodynamic loading is negligible. This bodes well for many flow-control applications, including separation control and suppression of flow-induced cavity oscillations. Of course, the effectiveness of flap-type actuators (and the corresponding scaling laws) in nonequilibrium boundary layers will be more complex and therefore requires further study.

Conclusions

This paper focused on design models suitable for the development of piezoelectric unimorph flap actuators that produce significant flow disturbances in low-speed flows at frequencies ranging from dc to their natural frequency. A composite beam model combined with an optimization method was used to design the actuators. Although the beam model is not capable of capturing all details of the actuator behavior, such as anticlastic curvature, the design tools were shown to adequately represent the observed experimental behavior of the actuator midplane tip. Such a simple model helps the designer to understand the causal relationship between design variables and actuator performance. However, more sophisticated tools, such as an analytical plate or a finite element model, will be better suited to study more complex geometries.

A sample application to open-loop control of separated flow from a backward-facing step at low subsonic speeds was illustrated. A fluid-structure-coupling model was hypothesized that accurately relates the generated streamwise velocity perturbation in the flow to the displacement characteristics of the actuator and the mean velocity profile. In particular, if the period of the forced oscillation is large compared to the characteristic convective time scale of the boundary layer, then the boundary layer is effectively displaced in the vertical direction because of the quasi-static motion of the actuator. This model led to a proposed scaling law relating the flap tip displacement and the incoming equilibrium turbulent boundary-layer profile to the streamwise velocity fluctuations produced by the actuator. These results are expected to be useful in the preliminary design of actuators for flow-control applications.

Appendix A: Governing Equations in Matrix Form

This section provides the matrix form of the governing equations. The solution in section 1 of the composite beam (see Fig. 1) is given by Eq. (4). Similarly, the solution in section 2 is given by Eq. (7). The eight unknown coefficients $a_1, a_2, \ldots, a_8$ are determined by the four boundary conditions given in Eq. (8). The four matching conditions at the junction of the two sections $x = L_p$ are given by Eq. (9). Applying these conditions leads to the following matrix equation:

$$D \cdot A = b$$

where

$$A^T = [a_1 \quad a_2 \quad a_3 \quad a_4 \quad a_5 \quad a_6 \quad a_7 \quad a_8]$$

$$b^T = [0 \quad 0 \quad 0 \quad 0 \quad 0 \quad 0 \quad M_0 \quad 0]$$

$$A = \begin{bmatrix} 1 & 1 & 1 & 1 & 0 & 0 & 0 & 0 \\ j & -j & 1 & -1 & 0 & 0 & 0 & 0 \\ 0 & 0 & 0 & 0 & e^{j\beta_2 L_s} & e^{-j\beta_2 L_s} & -e^{\beta_2 L_s} & -e^{-\beta_2 L_s} \\ 0 & 0 & 0 & 0 & je^{j\beta_2 L_s} & -je^{-j\beta_2 L_s} & -e^{\beta_2 L_s} & e^{-\beta_2 L_s} \\ e^{j\beta_1 L_p} & e^{-j\beta_1 L_p} & e^{\beta_1 L_p} & e^{-\beta_1 L_p} & -e^{j\beta_2 L_p} & -e^{-j\beta_2 L_p} & -e^{\beta_2 L_p} & -e^{-\beta_2 L_p} \\ j\beta_1 e^{j\beta_1 L_p} & -j\beta_1 e^{-j\beta_1 L_p} & \beta_1 e^{\beta_1 L_p} & -\beta_1 e^{-\beta_1 L_p} & -j\beta_2 e^{j\beta_2 L_p} & j\beta_2 e^{-j\beta_2 L_p} & -\beta_2 e^{\beta_2 L_p} & \beta_2 e^{-\beta_2 L_p} \\ -K_1\beta_1^2 e^{j\beta_1 L_p} & -K_1\beta_1^2 e^{-j\beta_1 L_p} & K_1\beta_1^2 e^{\beta_1 L_p} & K_1\beta_1^2 e^{-\beta_1 L_p} & K_2\beta_2^2 e^{j\beta_2 L_p} & K_2\beta_2^2 e^{-j\beta_2 L_p} & -K_2\beta_2^2 e^{\beta_2 L_p} & -K_2\beta_2^2 e^{-\beta_2 L_p} \\ -jK_1\beta_1^3 e^{j\beta_1 L_p} & jK_1\beta_1^3 e^{-j\beta_1 L_p} & K_1\beta_1^3 e^{\beta_1 L_p} & -K_1\beta_1^3 e^{-\beta_1 L_p} & jK_2\beta_2^3 e^{j\beta_2 L_p} & -jK_2\beta_2^3 e^{-j\beta_2 L_p} & -K_2\beta_2^3 e^{\beta_2 L_p} & K_2\beta_2^3 e^{-\beta_2 L_p} \end{bmatrix}$$

$$K_1 = E_s I_{s1} + E_p I_{p1}, \qquad K_2 = E_s I_{s2}$$

References

[1]Gad-el-Hak, M., "Modern Developments in Flow Control," *Applied Mechanics Review*, Vol. 49, No. 7, 1996, pp. 365–379.

[2]Wehrmann, O. H., "Reduction of Velocity Fluctuations in a Kármán Vortex Street by a Vibrating Cylinder," *Physics of Fluids*, Vol. 8, 1965, pp. 760, 761.

[3]Wehrmann, O. H., "The Influence of Vibrations on the Flow Field Behind a Cylinder," Boeing Scientific Research Lab., Document D1-82-0619, 1967.

[4]Wehrmann, O. H., "Self-Adjusting Feedback Loop for Mechanical Systems to Influence Flow in Transition. Part I," Boeing Scientific Research Lab., Document D1-82-0632, 1967.

[5]Wiltse, J. M., and Glezer, A., "Manipulation of Free Shear Flows Using Piezoelectric Actuators," *Journal of Fluid Mechanics*, Vol. 249, April 1993, pp. 261–285.

[6]Jacobson, S. A., and Reynolds, W. C., "Active Control of Streamwise Vortices and Streaks in Boundary Layers," *Journal of Fluid Mechanics*, Vol. 360, April 1998, pp. 179–211.

[7]Rathnasingham, R., and Breuer, K. S., "Coupled Fluid-Structural Characteristics of Actuators for Flow Control," *AIAA Journal*, Vol. 35, No. 5, 1997, pp. 832–837.

[8]Pan, J., Hansen, C. H., and Snyder, S. D., "A Study of the Response of a Simply Supported Beam to Excitation by a Piezoelectric Actuator," *Journal of Intelligent Material Systems and Structures*, Vol. 3, Jan. 1992, pp. 3–16.

[9]Söderkvist, J., "Dynamic Behavior of a Piezoelectric Beam," *Journal of the Acoustical Society of America*, Vol. 90, Pt. 1, No. 2, 1991, pp. 686–692.

[10]Miller, S. E., and Hubbard, J., "Theoretical and Experimental Analysis of Spatially Distributed Sensors on a Bernoulli-Euler Beam," The Charles Stark Draper Lab., CSDL C-5953, Cambridge, MA, 1987.

[11]Timoshenko, S., and Young, D. H., *Elements of Strength of Materials*, 4th ed., D. Van Nostrand Company, Princeton, NJ, 1962, pp. 111–117.

[12]Crawley, E. F., and de Luis, J., "Use of Piezoelectric Actuators as Elements of Intelligent Structures," *AIAA Journal*, Vol. 25, No. 10, 1987, pp. 1373–1385.

[13]Won, C. C., "Active Control of Smart Structures: Theory and Experiment," Ph.D. Dissertation, Dept. of Aerospace Engineering, Georgia Inst. of Technology, Atlanta, GA, Dec. 1990.

[14]Lagarias, J. C., Reeds, J. A., Wright, M. H., and Wright, P. E., "Convergence Properties of the Nelder-Mead Simplex Method in Low Dimensions," *SIAM Journal of Optimization*, Vol. 9, No. 1, 1998, pp. 112–147.

[15]Cimbala, J. M., and Park, W. J., "A Direct Hot-Wire Calibration Technique to Account for Ambient Temperature Drift in Incompressible Flow," *Experiments in Fluids*, Vol. 8, No. 5, 1990, pp. 299, 300.

[16]White, F. M., *Viscous Fluid Flow*, McGraw-Hill, New York, 1974, Chap. 6.

J. C. Hermanson
Associate Editor